PHYSICAL REVIEW A VOLUME 47, NUMBER 1 JANUARY 1993

$Ba(6s6p\ ^1P_{1,m_j}) \rightarrow Ba(6s6p\ ^3P_{2,m_j'})$ Zeeman cross sections in single collisions with N_2, O_2, and H_2

J.-M. Mestdagh, P. Meynadier, P. de Pujo, O. Sublemontier,
J.-P. Visticot, J. Berlande, J. Cuvellier, and T. Gustavsson*
Service des Photons, Atomes et Molécules, Centre d'Etudes Nucléaires de Saclay,
91191 Gif-sur-Yvette CEDEX, France

A. G. Suits† and Y. T. Lee
Department of Chemistry, University of California, Berkeley, California 94720
and Chemical Sciences Division, Lawrence Berkeley Laboratory, University of California, Berkeley, California 94720

(Received 6 April 1992)

Zeeman cross sections $\sigma_{j,m_j \rightarrow j',m_j'}$ for the spin-changing $6s6p\ ^1P_1-6s6p\ ^3P_2$ transition of barium induced by single collisions with N_2, O_2, and H_2 have been measured using a crossed-beam apparatus. State-selective preparation of $6s6p\ ^1P_{1,m_j}$ and detection of $6s6p\ ^3P_{2,m_j'}$ was achieved using the laser excitation technique in the presence of a magnetic field that breaks the degeneracy of the magnetic sublevels. The results showed that the Zeeman cross sections $\sigma(^1P_{1,m_j} \rightarrow {}^3P_{2,m_j'})$ are fairly dependent upon m_j and m_j' for N_2 and H_2, whereas the Zeeman cross sections all have the same value with O_2. Additionally the flux-velocity contour map of $Ba(6s6p\ ^3P_2)$ for scattering with H_2 depends significantly upon the magnetic sublevel of barium in the exit channel. The results for Ba-(N_2,H_2) scattering were accounted for semiquantitatively by a very simple model. The model was then used to stress which physical phenomena are at the origin of the preservation of the orbital alignment and orientation during collisions. The present work also compared the kind of information obtained by the direct measurement of Zeeman cross sections to that found in other experiments that deal with the effect of polarizing the collision partners.

PACS number(s): 34.50.Pi, 32.60.+i

I. INTRODUCTION

Collision physics of short-lived excited atomic states is a very-well-developed activity that takes its motivations into laser physics and atmospheric and combustion chemistry. Since excited states usually have nonzero momenta, it is useful to consider their polarization before and after the collision. Well-documented polarization effects concern the effect of initial polarization of the collision partners on the cross sections of scattering processes. Such effects are very interesting to study since they carry much detailed information about collision dynamics and interaction potentials. Several review papers highlight the subject [1–3]. Although less extensively documented, polarization effects have two further interesting aspects: collision-induced polarization and collisional transfer of initial orbital polarization into polarization of the collision products.

There are two different experimental approaches to these studies. The first, and the most widely reported one, is orbital selection through polarized excitation [4–11] (only the most recent works are quoted here, and the reader is referred to the review papers [1–3] for previous references). The second approach, the one that we followed along the present work, is based on the Zeeman effect. Orbital-selective *excitation and detection* is allowed by the splitting of the magnetic sublevels when a static magnetic field is applied to the atomic system. To our knowledge, only a few studies make use of this second approach and, with two exceptions, they all focus on intramultiplet collisional relaxation of excited alkali-metal atoms [12–18].

Spin-changing transitions between ^1P and ^3P electronic states of alkaline-earth-metal atoms in collisions with noble gases, and especially alignment effects in these collisions, have attracted much attention in recent years, both on the experimental and on the theoretical sides [3,19–23]. One of the main advantages of alkaline earth atoms over alkali-metal atoms, when studying polarization effects experimentally, is their zero nuclear spins that allow for very pure orbital preparations, and therefore lead to easily measurable effects. Only a few works have considered collisions of ^1P alkaline-earth-metal atoms with molecular partners [24,25].

The present paper reports on measurements of cross sections for spin-changing transitions $6s6p\ ^1P_{1,m_j} \rightarrow 6s6p\ ^3P_{2,m_j'}$ of barium, induced collisionally by molecules. These cross sections were resolved, Zeeman sublevel by Zeeman sublevel, in both the entrance channel and the exit channel. This work was performed using a crossed-beam apparatus, and the molecular perturbers under investigation were N_2, O_2, and H_2. The present investigation aims to document the dynamics of these collisions. In particular, it aims to discuss which physical phenomena are at the origin of the various aspects of polarization effects: namely, (i) effect of initial polarization of barium on the $6s6p\ ^1P_1 \rightarrow 6s6p\ ^3P_2$ collision cross section, (ii) transfer of the initial polarization of barium into the collision product Ba($6s6p\ {}^3P_2$), and (iii) induction of polarization into collision product Ba($6s6p\ {}^3P_2$) by the collision itself in the abscence of initial polarization of barium. Finally, the present work also compared the information provided by standard polarization-effect experiments, where only polarization in the entrance channel is controlled, to the present measurement of Zeeman cross sections where Zeeman sublevels are selected both in the entrance channel and in the exit channel of the collision.

Interestingly, a work has appeared in the literature when revising the present paper [26]. It addresses the question of spin-changing transitions ${}^1P_{1,m_j} \rightarrow {}^3P_{2,m_j'}$ in a way complementary to that developed here. The initial and final m_j sublevels were controlled by playing with the polarization of both the pump laser and the probe laser, and no magnetic field were used. The system considered by these authors is Ca-He, i.e., a much simpler system than the Ba-molecule systems investigated here.

Section II of the present paper describes the experimental apparatus and gives the principle of the experiment. The experimental results are shown in Sec. III. Section IV provides a very simple model of the Ba-N_2 scattering that helps the discussion of Sec. V. Finally, two appendices contain the mathematics used in the main course of the paper. Appendix A deals with the important question of optical pumping and coherent saturation in the measurement, and Appendix B shows how the model of Sec. IV is derived.

II. EXPERIMENT

A. Experimental apparatus

The experiment was run using a crossed-beam setup that has been described in detail elsewhere [27]. Briefly, an effusive barium beam was crossed at 90° by a supersonic molecular beam, and single-collision conditions were achieved. Care was also taken so that no clusters were present in the molecular beam.

The ^{138}Ba($6s6p\ {}^1P_1$) state was pumped by a frequency-stabilized cw ring dye laser (Spectra-Physics 360 running with Rhodamine 560). The m_j selective preparation of the Ba($6s6p\ {}^1P_1$) state was achieved by applying a weak magnetic field of 700 G at an angle of 45° to the two particle beams, as shown in Fig. 1. Likewise, m_j' selective probing of the $6s6p\ {}^3P_2$ state population was made possible by a high-resolution laser excitation spectrum of the $6s6p\ {}^3P_2 \rightarrow 6s7s\ {}^3S_1$ transition, with all the Zeeman lines resolved. For this purpose a second dye laser system, similar to the first one but running with LD700 dye, was used. The laser excitation scheme is illustrated in Fig. 2.

The two laser beams were directed colinearly into the collision zone by an optical fiber perpendicular to the plane of the two molecular beams. The laser beams were not polarized at the output of the fiber. As a result each laser can perform an electronic excitation requiring either linear (i.e., π), clockwise circular (i.e., σ^+), or counterclockwise circular (i.e., σ^-) polarization. The π photons are associated with one half of the total laser power, and the σ photons with the other half, i.e., one quarter for σ^+ and one quarter for σ^-.

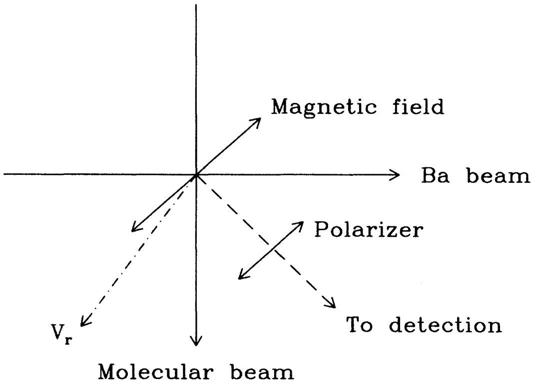

FIG. 1. Scheme of the apparatus.

The detection is performed by analyzing the fluorescence coming from the level $6s7s\ {}^3S_1$ at 90° to the magnetic field, in the plane of the two particle beams (see Fig. 1). A monochromator coupled to an RCA-31034 photomultiplier tube is used for this purpose, and a polarizer is added to detect π-type fluorescence of either the $6s7s\ {}^3S_1 \rightarrow 6s6p\ {}^3P_1$ or $6s7s\ {}^3S_1 \rightarrow 6s6p\ {}^3P_0$ transitions.

B. Data acquisition

The pump laser was tuned for preparation of Ba($6s6p\ {}^1P_1$), either with $m_j=0$ or with $m_j=+1$ (for symmetry reasons, as far as total cross sections are concerned, the preparation of $m_j=-1$ yields the same information as preparation of $m_j=+1$). For each preparation, the probe laser was scanned across the $6s6p\ {}^3P_2 \rightarrow 6s7s\ {}^3S_1$ multiplet, and was operated under the saturation regime described in Appendix A. A Fabry-Pérot interferometer helped to monitor the scanning. The laser-induced fluorescence (LIF) signals coming from either $6s7s\ {}^3S_1 \rightarrow 6s6p\ {}^3P_1$ or $6s7s\ {}^3S_1 \rightarrow 6s6p\ {}^3P_0$ transitions were recorded. This resulted in two LIF spectra for each preparation of the $6s6p\ {}^1P_1$ level $m_j=0$ and $+1$. Because of the polarizer placed in the

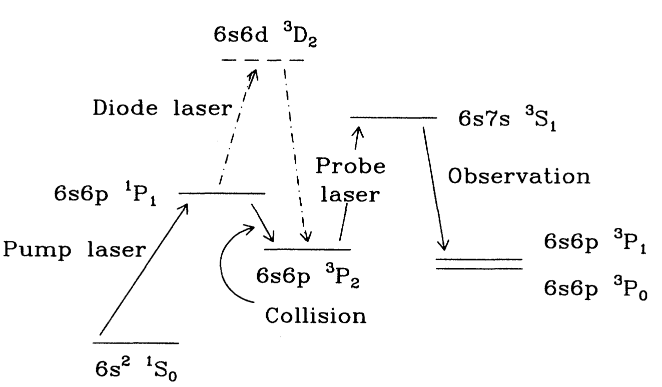

FIG. 2. Energy levels of barium. The solid arrows show the principle of the measurement. The dashed arrows document the control experiment performed using the diode laser (see Appendix A).

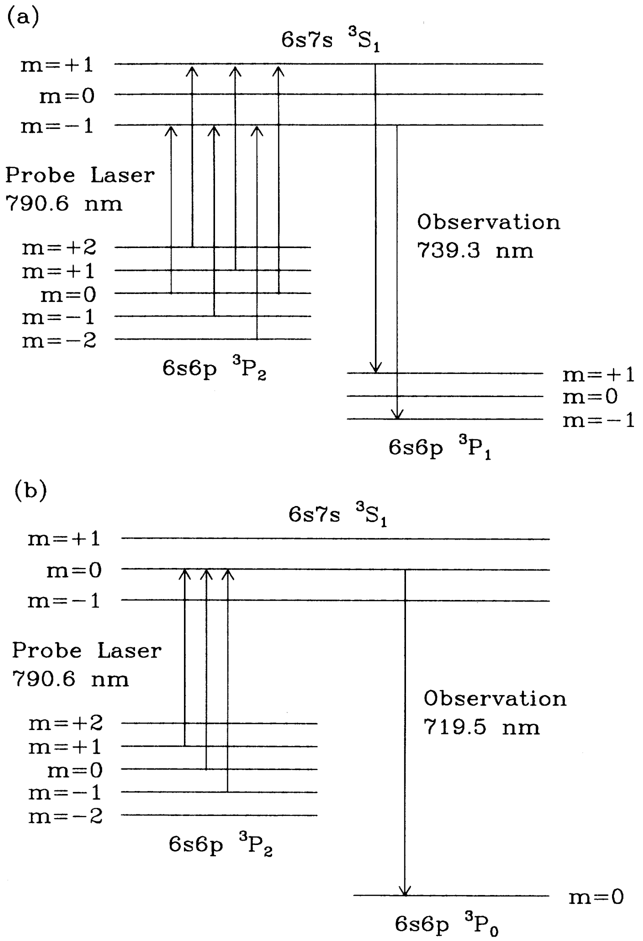

FIG. 3. Energy levels of barium split by a magnetic field. (a) shows the detection scheme when π-type fluorescence is observed for the $6s7s\ {}^3S_1\rightarrow 6s6p\ {}^3P_1$ transition. (b) corresponds to π-type fluorescence detection of the $6s7s\ {}^3S_1\rightarrow 6s6p\ {}^3P_0$ transition.

detection line, LIF spectra recorded with the $6s7s\ {}^3S_1\rightarrow 6s6p\ {}^3P_1$ detection contained six lines. From the red side to the blue side of the spectra, these six lines corresponded to the transitions ${}^3P_{2,0}\rightarrow {}^3S_{1,-1}$, ${}^3P_{2,+2}\rightarrow {}^3S_{1,+1}$, ${}^3P_{2,-1}\rightarrow {}^3S_{1,-1}$, ${}^3P_{2,+1}\rightarrow {}^3S_{1,+1}$, ${}^3P_{2,-2}\rightarrow {}^3S_{1,-1}$, and ${}^3P_{2,0}\rightarrow {}^3S_{1,+1}$. The LIF signal thus came in this case from the decay of $6s7s\ {}^3S_{1,m_j''=\pm 1}$ only.

In the same way, the spectra recorded with the $6s7s\ {}^3S_1\rightarrow 6s6p\ {}^3P_0$ detection had three lines corresponding to the decay of $6s7s\ {}^3S_{1,m_j''=0}$: ${}^3P_{2,+1}\rightarrow {}^3S_{1,0}$, ${}^3P_{2,0}\rightarrow {}^3S_{1,0}$, and ${}^3P_{2,-1}\rightarrow {}^3S_{1,0}$ transitions from the red end to the blue end of the spectra. The detection scheme is summarized in Fig. 3.

Other spectra, which are not shown in Sec. III, below, were taken with the probe laser tuned to detect a given Zeeman sublevel of $6s6p\ {}^3P_2$. The pump laser was then scanned across the $6s^2\ {}^1S_0\rightarrow 6s6p\ {}^1P_1$ multiplet. This allowed us to scale one to the other the spectra obtained when scanning the probe laser for the two preparations $m_J=0$ and $m_j'=+1$ of $\mathrm{Ba}(6s6p\ {}^1P_1)$. Furthermore, the data taken with both pump and probe lasers scanned are redundant. This allowed us to double check several relative values between the Zeeman cross sections $\sigma(6s6p\ {}^1P_{1,m_j}\rightarrow 6s6p\ {}^3P_{2,m_j'})$ under consideration.

C. Data analysis

The detection of scattered barium atoms in the $6s6p\ {}^3P_2$ level goes through a laser-induced fluorescence measurement. Let us name $I_{\mathrm{LIF}}(m_j,m_j')$ the signal measured when collisions of the $6s6p\ {}^1P_{1,m_j}$ level are studied, and when the magnetic sublevel $6s6p\ {}^1P_{2,m_j'}$ is probed. $I_{\mathrm{LIF}}(m_j,m_j')$ is proportional to the desired Zeeman cross section $\sigma(6s6p\ {}^1P_{1,m_j}\rightarrow 6s6p\ {}^3P_{2,m_j'})$ and to the detection efficiency $\phi(m_j',J)$ of the m_j' level. The cross section is thus given by

$$\sigma(6s6p\ {}^1P_{1,m_j}\rightarrow 6s6p\ {}^3P_{2,m_j'})\sim\frac{I_{\mathrm{LIF}}(m_j',J)}{\phi(m_j',J)}\ . \tag{1}$$

Appendix A shows that the detection efficiency $\phi(m_j',J)$ used in expression (1) both depends on the magnetic sublevel m_j' that is probed and on the transition $6s7s\ {}^3S_1\rightarrow 6s6p\ {}^3P_J$ (with $J=0$ or 1) to which the detection is tuned. Appendix A provides calculations and experimental measurements of these efficiencies. The results are listed in Table I.

III. RESULTS

The spectra that were recorded when tuning the probe laser across the $6s6p\ {}^3P_2\rightarrow 6s7s\ {}^3S_1$ multiplicity are shown in Figs. 4–6, respectively for the molecular per-

TABLE I. Relative efficiencies for probing the population of the Zeeman sublevels m_j' of $6s6p\ {}^3P_2$. Calculated efficiencies are compared to those measured in the diode laser experiment (see the text). The $m_j'=0$ sublevel serves as a reference for calibration in each detection scheme: $6s7s\ {}^3S_1\rightarrow 6s6p\ {}^3P_1$ and $6s7s\ {}^3S_1\rightarrow 6s6p\ {}^3P_0$.

Level probed	$6s7s\ {}^3S_1\rightarrow 6s6p\ {}^3P_1$		$6s7s\ {}^3S_1\rightarrow 6s6p\ {}^3P_0$	
$6s6p\ {}^3P_2,m_j'$	Calculated	Measured	Calculated	Measured
$m_j'=\pm 2$	3.4	3.8±0.6	0	0
$m_j'=\pm 1$	2.8	3.1±0.5	0.6	0.7±0.1
$m_j'=0$	1	1	1	1

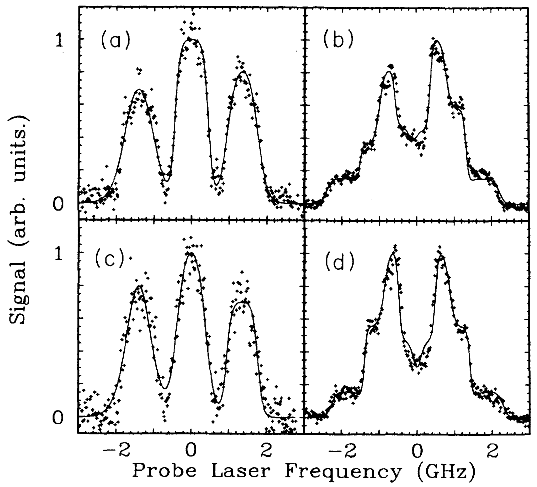

FIG. 4. Excitation spectrum of the $6s6p\,^3P_2 \rightarrow 6s7s\,^3S_1$ transition when the $6s6p\,^3P_2$ level is populated by collision of $Ba(6s6p\,^1P_1)$ with N_2. Panels (a) and (b) correspond to $6s6p\,^1P_{1,m_j=+1}$ excitation with the detection tuned to $6s7s\,^3S_1 \rightarrow 6s6p\,^3P_0$ in panel (a) and to $6s7s\,^3S_1 \rightarrow 6s6p\,^3P_1$ in panel (b). Panels (c) and (d) correspond to $6s6p\,^1P_{1,m_j=0}$ excitation. Panel (c) is associated with the $6s7s\,^3S_1 \rightarrow 6s6p\,^3P_0$ detection, and panel (d) with the $6s7s\,^3S_1 \rightarrow 6s6p\,^3P_1$ detection.

turbers N_2, O_2, and H_2. As anticipated in Sec. II, three lines are observed when tuning the detection to the $6s7s\,^3S_1 \rightarrow 6s6p\,^3P_0$ transition, and six lines are observed when tuning it to $6s7s\,^3S_1 \rightarrow 6s6p\,^3P_1$. The spacing between these lines allows one to notice that the ratio between the Landé factor of $6s7s\,^3S_1$ and that of $6s6p\,^3P_2$ is 0.77 ± 0.03, i.e., equal within experimental uncertainties to the value of 0.75 that is expected from pure *LS* coupling [28].

The raw data provided by Figs. 4–6 then were treated

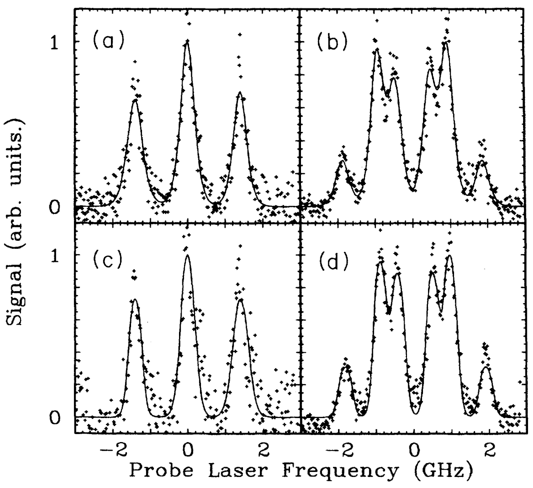

FIG. 5. Same caption as Fig. 4, but the collision partner of Ba is O_2.

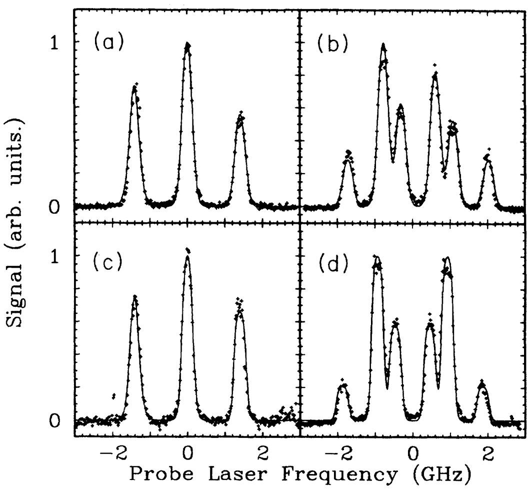

FIG. 6. Same caption as Fig. 4, but the collision partner of Ba is H_2.

as follows. Integrated line profiles of the separate Zeeman lines were evaluated by fitting a synthetic line spectrum to the experimental one by standard nonlinear methods and integrating the corresponding line shapes. The well-resolved Zeeman lines in the $Ba(6s6p\,^1P_1)+O_2,H_2$ cases were described by Lorenzian line profiles. In the $Ba(6s6p\,^1P_1)+N_2$ case, the individual line profiles were much broader and partly overlapping, and were described by smooth rectangles that were generated using hyperbolic tangent functions. The integrated line profiles, i.e., the LIF signal, were related to the collision cross sections using Eq. (1). The results are given in Figs. 7–9. Zeeman cross sections

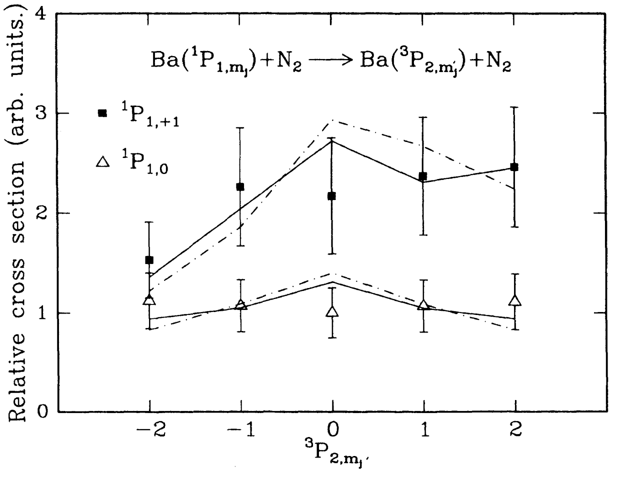

FIG. 7. Zeeman cross sections $\sigma_{j,m_j \rightarrow j',m_j'}$ for the transition $6s6p\,^1P_1 \rightarrow 6s6p\,^3P_2$ of Ba induced by N_2. The initial preparation of $6s6p\,^1P_1$ is indicated in the figure. For the clarity of the figure, the calculations reported in Sec. IV are shown as broken lines, although m_j' only takes integral values. The solid and dotted-dashed lines correspond, respectively, to bent and straight trajectories.

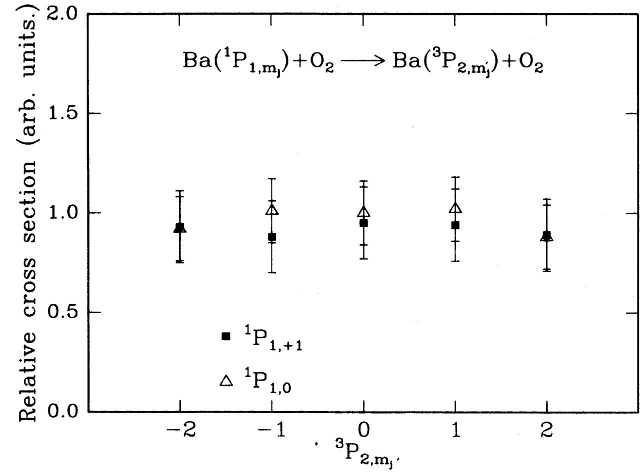

FIG. 8. Same caption as Fig. 7, but the collision partner of Ba is O_2, and no calculation is reported.

$\sigma(6s6p\ ^1P_{1,m_j} \rightarrow 6s6p\ ^3P_{2,m_j'})$ are fairly dependent upon m_j and m_j' for N_2 and H_2, whereas the Zeeman cross section all have the same value with O_2.

The shape of the peaks in the spectra of Figs. 4–6 are very different from one molecular perturber to the other. The peaks are very sharp for H_2 (Fig. 6), much broader for O_2 (Fig. 5), and very much overlapping for N_2 (Fig. 4). The width of each peak is for one part, the result of power broadening due to saturation by the probe laser, and for the other part the result of Doppler broadening due to the distribution of recoil velocities of the scattered barium atoms along the direction of the probe laser. The relation that exists between the shape of laser-induced fluorescence peaks and velocity distributions of the detected product has been examined in the case where the collision induced energy transfer $6s6p\ ^1P_1 \rightarrow 6s6p\ ^3P_2$ is not resolved Zeeman level by Zeeman level [25]. In this case, only one peak is detected when scanning the probe laser. It corresponds to the superposition of the $3+6=9$ peaks observed in the present work for each gas. It has been shown in [25] that the shape of this peak contains information about the flux-velocity contour map of collision product $Ba(6s6p\ ^3P_2)$, and how to extract this information when the probe laser operates under the nonsaturation regime.

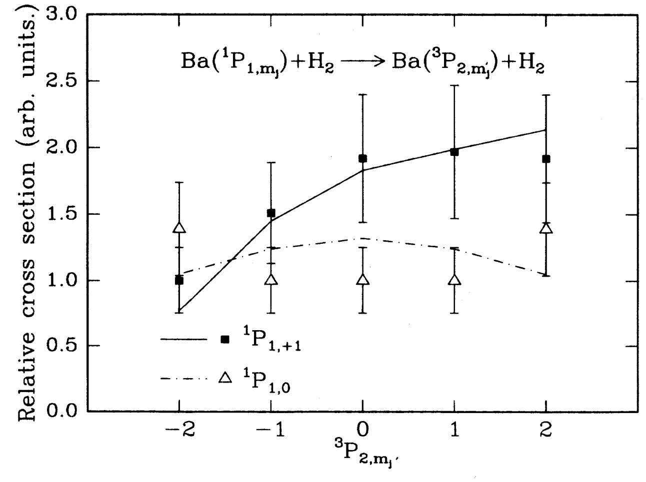

FIG. 9. Same caption as Fig. 7, but the collision partner of Ba is H_2.

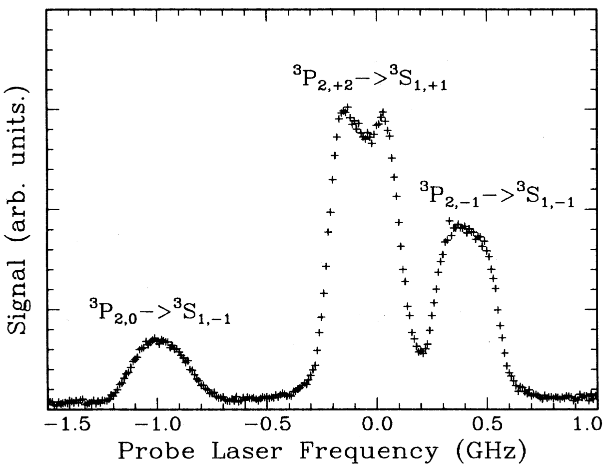

FIG. 10. Excitation spectrum of the $6s6p\ ^3P_2 \rightarrow 6s7s\ ^3S_1$ transition when the $6s6p\ ^3P_2$ level is population by collision of $Ba(6s6p\ ^1P_{1,m_j=0})$ with H_2. The detection scheme is that shown in Fig. 3(a), and the probe laser operates in the nonsaturation regime.

The power broadening is too large in the peaks of Figs. 4–6 to give accurate information about flux-velocity contour maps with selected Zeeman sublevels of the initial and final levels of barium. We attempted, however, to get this information by lowering the power of the probe laser so that the power broadening becomes negligible. This results in much lower signals, and the experiment could be conducted with H_2 only. The corresponding spectrum is shown in Fig. 10. The detection was tuned to the $6s7s\ ^3S_1 \rightarrow 6s6p\ ^2P_1$ transition, and the probe laser was scanned across the red half of the $6s6p\ ^3P_2 \rightarrow 6s7s\ ^3S_1$ multiplet. The shape of the peak corresponding to the $6s6p\ ^3P_{2,+2} \rightarrow 6s7s\ ^3S_{1,+1}$ transition is distinctly different from that of the two other peaks.

IV. MODEL OF THE SPIN-CHANGING COLLISION $Ba(6s6p\ ^1P_1 \rightarrow 6s6p\ ^3P_2)/N_2H_2$

This section proposes a framework to discuss the results of the previous section without entering into complicated calculations of potential surfaces and collision dynamics. Emphasis is given to Ba-N_2 scattering, but most of the results apply for H_2 as well. The section is split into two parts. First, it provides a guess of interaction potentials for the Ba-N_2 pair, and second it accounts for the collision process in a very simple way so as to examine which physical phenomena affect the relative value of Zeeman cross sections.

A. Potentials

The spin-changing transition Ba($6s6p\ ^1P_1 \rightarrow 6s6p\ ^3P_2$) induced by collision with argon atoms has been studied recently in our laboratory [20], and a mechanism based on simple curve crossings has been proposed. The collision mechanism is likely to be the same when the argon perturber is replaced with N_2 under collinear geometry. In both cases, the potential curves have the symmetry provided by the $C_{\infty v}$ point group, and the interaction of Ba with N_2 under collinear geometry should not differ too much from that of Ba with Ar. The potential-energy curves postulated in our earlier work on Ba+Ar are thus used here to describe the Ba-N_2 interaction under the collinear approach. The curves are shown in Fig. 11(a), and the way they have been obtained is explained in Appendix B.

The spin-changing transition $6s6p\ ^1P_1 \rightarrow 6s6p\ ^3P_2$ is due essentially to the crossing (indicated by a circle in the figure) between the $^1\Pi_1$ curve correlating to Ba($6s6p\ ^1P_1$) and the strongly repulsive $^3\Sigma_1$ curve correlating to Ba($6s6p\ ^3P_2$). Such a transfer is not allowed in the absence of spin-orbit coupling, but the large spin-orbit interaction due to the presence of barium makes possible mixing between $\Omega=1$ molecular states of different multiplicity.

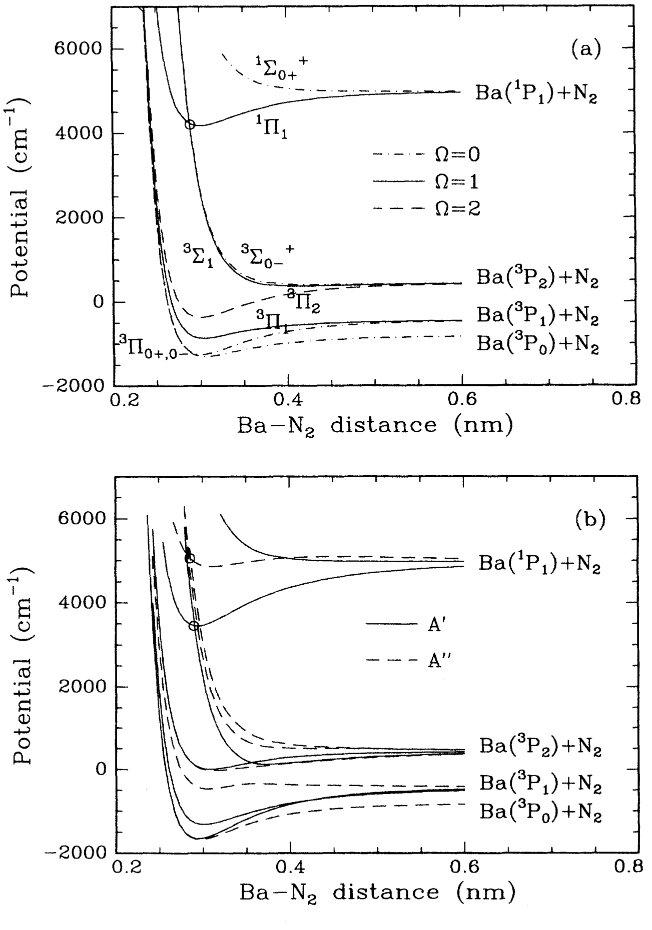

FIG. 11. Scheme of the Ba-Ar (a) and Ba-N_2 (b) potential-energy curves correlating to the $6s6p\ ^{1,3}P$ states of barium. (a) is based on data from Ref. [20].

Of course, the collision only has a vanishing probability to occur under pure $C_{\infty v}$ geometry. It is better described by the C_s point group, which has a lower symmetry than $C_{\infty v}$. As a result, the degenerate potential curves of the $C_{\infty v}$ point group corresponding to $\Omega \neq 0$ are split into two branches of A' and A'' symmetry. One is the symmetric combination of $+\Omega$ and $-\Omega$ states, and the other one is the antisymmetric combination. Moreover, the selection rules governing the collision in the $C_{\infty v}$ point group ($\Delta\Omega=0, + \leftrightarrow +$, and $- \leftrightarrow -$) are lowered to $A' \leftrightarrow A'$, $A'' \leftrightarrow A''$. The number of potential branches that are coupled and the number of coupling regions are thus enhanced. Fortunately, a full description of the Ba-N_2 interaction surfaces is not required to roughly localized these couplings. It is enough to consider potential curves that represent the average Ba-N_2 interaction. This was achieved by applying the approach described by Hickman for alkali metal ($np\ ^2P$)−H_2,N_2 systems to the Ba($6s6p\ ^1P$)−N_2 and Ba($6s6p\ ^3P$)−N_2 pairs [29].

The details of the calculations are given in Appendix B, and the corresponding potential curves are shown in Fig. 11(b). The potential curves are labeled as under C_s symmetry. The two circles in the figure indicate the location of the crossings between singlet and triplet curves that are responsible for most of the spin-changing transition $6s6p\ ^1P_1 \rightarrow 6s6p\ ^3P_2$. The upper crossing couples the $1\ ^1A''$ curve with the $4\ ^3A''$, and $5\ ^3A''$ curves. The lower crossing couples the $1\ ^1A'$ curve to $4\ ^3A'$. It must be noticed that the coupling between the $1\ ^1A''$ and $4\ ^3A''$ curve has no equivalent under the $C_{\infty v}$ point group, since it violates the $\Delta\Omega=0$ selection rule.

The calculations also provide the character of each Ba-N_2 molecular level in terms of atomic orbitals of Ba as a function of the Ba-N_2 distance. Table II lists the character of several molecular levels when the separation between Ba and N_2 is large (10 Å). Such information will be useful in Sec. IV B below when constructing the collision model. The character of the same levels at smaller Ba-N_2 separations would allow one to evaluate the force of the spin-orbit coupling between singlet and triplet curves at each crossing. However, it is enough for the present purpose to assume that the singlet curves are efficiently coupled to the triplet curves at each crossing.

Switching from N_2 to H_2 leaves the gross features of the potentials unaffected. Owing to its smaller anisotropy, the splitting between A' and A'' curves would be smaller with H_2 for those curves that are degenerated under the $C_{\infty v}$ point group. However, the character of the molecular level listed in Table II would stay the same.

B. Collision model

The collision is conveniently divided into five steps:

(i) At large separation between barium and N_2, the laser-excited Ba · · · N_2 molecular orbitals that correlate to Ba($6s6p\ ^1P_{1,m_j}$)+N_2 closely resemble barium atomic

TABLE II. The Ba-N_2 molecular states $1\ {}^1A'$, $1\ {}^1A''$, $4\ {}^3A'$, $4\ {}^4A''$, $5\ {}^3A''$ are those involved in the curve crossings shown in Fig. 11(b). The table gives their composition as percentages of atomic orbitals of barium. These compositions refer to a Ba-N_2 separation of 10 Å.

Molecular levels	${}^1P_{1,+1}$	${}^1P_{1,-1}$	${}^3P_{2,+2}$	${}^3P_{2,+1}$	${}^3P_{2,0}$	${}^3P_{2,-1}$	${}^3P_{2,-2}$
$1\ {}^1A'$	50%	50%					
$4\ {}^3A'$				50%		50%	
$1\ {}^1A''$	50%	50%					
$4\ {}^3A''$			25%		50%		25%
$5\ {}^3A''$				50%		50%	

orbitals. They are not efficiently coupled to the rotating Ba-N_2 molecular plane, nor to the axis **Z** connecting Ba to the center of mass of N_2. Therefore, the Ba $\cdots$ N_2 orbitals stay space fixed as the collision proceeds. The convenient reference frame in this case has its **z** axis along the relative velocity $\mathbf{V}_r$. The other two axes **x** and **y** of the $\{\mathbf{x},\mathbf{y},\mathbf{z}\}$ reference frame can be chosen at will.

(ii) At a certain distance, the electrostatic interaction between Ba and N_2 is large enough to overcome the Coriolis coupling due to the rotation of the Ba-N_2 system as the collision proceeds. The atomic orbital first locks to the Ba-N_2 axis **Z** and follows its rotation. Then, on closer approaches, the excited orbital feels the anisotropy of N_2. It then locks to the Ba-N_2 molecular plane itself, and follows its rotation. After this step of the collision, the Ba $\cdots$ N_2 orbitals stay body fixed, and are best represented by the molecular levels shown in Fig. 11(b) instead of the atomic orbitals used at step (i). The convenient reference frame is then $\{\mathbf{X},\mathbf{Y},\mathbf{Z}\}$, where **Z** is already defined. **X** is chosen perpendicular to the Ba-N_2 molecular plane. Symmetries A' and A'' of the molecular levels shown in Fig. 11(b) correspond to even and odd reflection symmetries with respect to the plane $(\mathbf{Y},\mathbf{Z})$.

These two steps of the collision refer to the concept of "locking radius" that was firmly established in atom-atom collisions [1,23,30]. This concept is the equivalent in collision physics to a switch from Hund's coupling case "*e*" to "*c*" in molecular physics. This concept is extended here to atom-molecule collisions, in very much the same way as was done before for Na($3P$)-N_2 quenching [1]. The most important approximation here was to assume that step (ii) is sudden.

At step (i) the density matrix describing the Ba-N_2 system is well approximated by the density matrix describing the pure atomic state Ba($6s6p\ {}^1P_{1,m_j}$) that was populated by the laser excitation. The only nonzero term of this matrix is $\rho({}^1P_1)_{m_j,m_j}=1$. Of course, the reference frame used is $\{\mathbf{x},\mathbf{y},\mathbf{z}\}$. At step (ii), the reference frame must be rotated from $\{\mathbf{x},\mathbf{y},\mathbf{z}\}$ to $\{\mathbf{X},\mathbf{Y},\mathbf{Z}\}$, and the density matrix must be expressed in terms of molecular energy levels of the Ba-N_2 system.

Let (α,β,γ) be the Euler angles that allow to rotate from old positions $\{\mathbf{x},\mathbf{y},\mathbf{z}\}$ to new positions $\{\mathbf{X},\mathbf{Y},\mathbf{Z}\}$. Angle α is the rotation about **z** that brings the **x** axis into the $(\mathbf{z},\mathbf{Z})$ plane, β is the angle between **z** and **Z**, and γ is the angle between the $(\mathbf{z},\mathbf{Z})$ plane and the Ba-N_2 plane. Neither the collision plane nor the Ba-N_2 plane is selected under the present experimental conditions. As a result, angles α and γ vary freely between 0 and 2π and must be averaged. After these rotation and averaging have been performed, the density matrix describing the system on the atomic basis $\{{}^1P_{1,0},{}^1P_{1,-1},{}^1P_{1,+1}\}$ in the $\{\mathbf{X},\mathbf{Y},\mathbf{Z}\}$ reference frame is given by

$$\rho'({}^1P_1)=\begin{bmatrix} d^{(1)}_{m_j,0}(\beta)^2 & 0 & 0 \\ 0 & d^{(1)}_{m_j,-1}(\beta)^2 & 0 \\ 0 & 0 & d^{(1)}_{m_j,+1}(\beta)^2 \end{bmatrix}, \tag{2}$$

where $d^{(j)}_{m,m'}(\beta)$ is a rotation matrix as defined by Brink and Satchler [31]. When projected on the molecular basis $\{2\ {}^1A',1\ {}^1A',1\ {}^1A''\}$, the same density matrix becomes

$$\rho'({}^1P_1)=\frac{1}{2}\begin{bmatrix} 2d^{(1)}_{m_j,0}(\beta)^2 & 0 & 0 \\ 0 & \mathcal{A}_{\text{sum}} & \mathcal{A}_{\text{diff}} \\ 0 & \mathcal{A}_{\text{diff}} & \mathcal{A}_{\text{sum}} \end{bmatrix} \tag{2'}$$

with

$$\mathcal{A}_{\text{sum}}=d^{(1)}_{m_j,+1}(\beta)^2+d^{(1)}_{m_j,-1}(\beta)^2\ ,$$

$$\mathcal{A}_{\text{diff}}=d^{(1)}_{m_j,+1}(\beta)^2-d^{(1)}_{m_j,-1}(\beta)^2\ .$$

(iii) After locking, the system can be considered as undergoing a coherent or partially coherent scattering on the three curves $1\ {}^1A'$, $2\ {}^1A'$, and $1\ {}^1A''$ correlating to $6s6p\ {}^1P_1$. Since these three curves do not have the same shape, some of the coherence is lost as the collision proceeds. The system then reaches the three regions of coupling between the singlet and triplet curves that we have encountered in Sec. IV A. Flux and coherence is totally or partly transferred to the triplet curves $4\ {}^3A'$, $4\ {}^3A''$, $5\ {}^3A''$ correlating to $6s6p\ {}^3P_2$ at these crossings. The collision then proceeds along the triplet curves until the unlocking. The barium atom is in the $6s6p\ {}^3P_2$ state, and is described by a density matrix noted $\rho'({}^3P_2)$. This matrix is conveniently represented on the basis of molecular states $\{3\ {}^3A'',3\ {}^3A',4\ {}^3A',4\ {}^3A'',5\ {}^3A''\}$ that correlate to Ba($6s6p\ {}^3P_2$)+N_2 in the $\{\mathbf{X},\mathbf{Y},\mathbf{Z}\}$ reference frame:

$$\rho'(^3P_2)=\frac{1}{2}\begin{bmatrix} 0 & 0 & 0 & 0 & 0 \\ 0 & 0 & 0 & 0 & 0 \\ 0 & 0 & \mathcal{A}_{\rm sum} & \frac{\lambda}{\sqrt{2}}\mathcal{A}_{\rm diff} & \frac{\lambda}{\sqrt{2}}\mathcal{A}_{\rm diff} \\ 0 & 0 & \frac{\lambda}{\sqrt{2}}\mathcal{A}_{\rm diff} & \frac{1}{2}\mathcal{A}_{\rm sum} & \frac{\lambda}{2}\mathcal{A}_{\rm diff} \\ 0 & 0 & \frac{\lambda}{\sqrt{2}}\mathcal{A}_{\rm diff} & \frac{\lambda}{2}\mathcal{A}_{\rm diff} & \frac{1}{2}\mathcal{A}_{\rm sum} \end{bmatrix} . \tag{3}$$

The writing of Eq. (3) assumes equal probability for the three couplings responsible for the spin-changing transfer. It contains a parameter λ that is ranging between 1 and 0 whether coherences are fully preserved or totaly destroyed during the collision.

(iv) The system then reaches the unlocking radius where the excited molecular orbital unlocks from the molecular plane. As in the entrance valley, such a behavior is conveniently taken into account by switching from the molecular basis to the atomic basis. The character of the molecular states $\{4\,^3A',4\,^3A'',5\,^3A''\}$ listed in Table II allowed us to express the matrix $\rho'(^3P_2)$ on the atomic basis $\{^3P_{2,-2},{}^3P_{2-1},{}^3P_{2,0},{}^3P_{2,+1},{}^3P_{2,+2}\}$. As we shall see below, only the diagonal elements of the matrix are needed. They are given by:

$$\begin{aligned} &\rho'(^3P_2)_{-2,-2}=\tfrac{1}{16}\mathcal{A}_{\rm sum}\,, \\ &\rho'(^3P_2)_{-1,-1}=\tfrac{3}{8}\mathcal{A}_{\rm sum}-\frac{1}{\sqrt{8}}\mathcal{A}_{\rm diff}\,, \\ &\rho'(^3P_2)0,0=\tfrac{1}{8}\mathcal{A}_{\rm sum}\,, \\ &\rho'(^3P_2)_{+1,+1}=\tfrac{3}{8}\mathcal{A}_{\rm sum}+\frac{1}{\sqrt{8}}\mathcal{A}_{\rm diff}\,, \\ &\rho'(^3P_2)_{+2,+2}=\tfrac{1}{16}\mathcal{A}_{\rm sum}\,. \end{aligned} \tag{3'}$$

(v) The system undergoes a depolarization in the final step of the collision that is accounted for by a rotation of the same angle β as in the entrance channel if assuming straight trajectories for the collisions. After this rotation, the system is expressed again in the initial reference frame $\{\mathbf{x},\mathbf{y},\mathbf{z}\}$. The populations transferred into the magnetic sublevels m_j' of the $6s6p\,^3P_2$ level by the collision are given by

$$\rho(^3P_2)_{m_j',m_j'}=\sum_M d^{(2)}_{m_j'M}(-\beta)d^{(2)}_{M,m_j'}(\beta)\rho'(^3P_2)_{M,M}\,. \tag{4}$$

The fact that only populations $\rho'(^3P_2)_{M,M}$ appear in Eq. (4) has the same origin as the presence of diagonal elements only in Eq. (2). It is due to the averaging to zero of all coherences when considering the cylindrical distribution of barium scattering about the relative velocity vector.

Expression (4) assumes straight trajectories for barium. However, our previous work on product angular distributions in $\mathrm{Ba}(6s6p\,^1P_1\rightarrow 6s6p\,^3P_2)-\mathrm{N}_2$ scattering has shown that Ba is scattered under a mean angle $\Theta=40°$ in the center-of-mass reference frame, with twice the velocity it had in the entrance channel. As a result, the impact parameter in the exit channel is half that in the entrance channel to ensure the conservation of angular momentum. Assuming an equal locking distance in both entrance and exit channels, we then conclude that the rotation between unlocking and exit is half the one considered above. Now, since the relative velocity of the reactant pair is 40° off the initial relative velocity, a further rotation by this amount must be done to express the density matrix in the initial reference frame.

The above "story" of the collision allows easy calculation for both the "exit scenarios" with straight and bent trajectories. This led us to calculate the final population of $6s6p\,^3P_{2,m_j'}$ sublevels for preparation of $6s6p\,^1P_1$ either with $m_j=+1$ or 0; i.e., it allows the derivation of relative values of the Zeeman cross sections $\sigma(6s6p\,^1P_{1,m_j}\rightarrow 6s6p\,^3P_{2,m_j'})$. The results are shown in Fig. 12.

A first prominent effect in Fig. 12 is the close resemblance between cross sections for straight and bent trajectories. This is due to compensation between the smaller rotation between unlocking and exit, and the additional rotation due to sideways scattering.

Another prominent effect is that due to the loss of coherence between A' and A'' curves as the collision proceeds. Memory of initial orientation is conserved when $\lambda=1$ and 0.5 for both rotation angles $\beta=\pi/5$ and $\pi/6$. The Zeeman cross section becomes symmetrical in $+m_j'$ and $-m_m'$ for the total loss of coherence ($\lambda=0$), as anticipated above. Another point merits attention: for

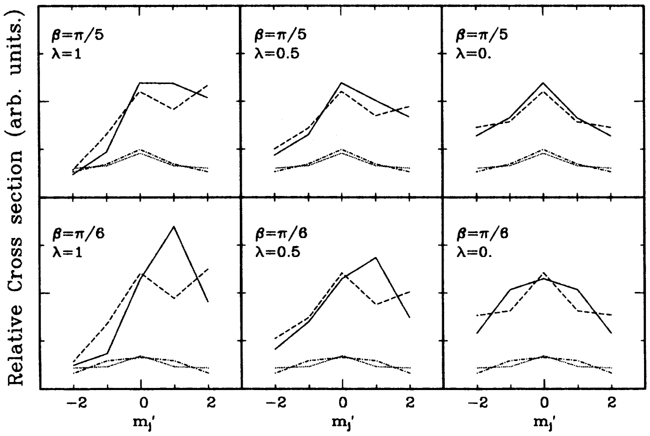

FIG. 12. Zeeman cross sections $\sigma_{j,m_j\rightarrow j',m_j'}$ calculated for the collision-induced transition $\mathrm{Ba}(6s6p\,^1P_1\rightarrow 6s6p\,^3P_2)$. For the clarity of the figure, the results are shown as broken lines although m_j' only takes integral values. The figure shows the effect of various phenomena. Initial preparation of $\mathrm{Ba}(6s6p\,^1P_1)$ in $m_j=+1$ corresponds to solid and dashed curves, and preparation in $m_J=0$ corresponds to dotted-dashed and dotted curves. Straight trajectories corresponds to solid and dotted-dashed curves, whereas bent trajectories with $\Theta=40°$ correspond to the dashed and dotted curves. Finally, the effect of varying both the rotation angle β before locking and the fraction of coherence conserved λ is also explored as labeled in each panel of the figure.

both rotation angles and both kinds of trajectories (straight or bent), the $m_j=+1$ sublevel leads to larger cross sections than $m_j=0$.

The present model served also to fit the experimental results for N_2 and H_2 in Figs. 7 and 9, respectively. However, a complication arises due to the fact that the direction of the magnetic field **B** is not parallel to the relative velocity vector $\mathbf{V}_r$. The angle between **B** and $\mathbf{V}_r$ is 17° in the Ba-N_2 experiment and 42° in the Ba-H_2 experiment. This must be accounted for by a further rotation of the density matrices $\rho(^1P_1)$ and $\rho(^3P_2)$ to bring them into a reference frame having its **z** axis along **B**. This complicates the writing of Eqs. (2)–(4) but does not affect the essence of the model.

For N_2, the best fit to experimental data shown in Fig. 7 was obtained with the rotation angle before locking equal to $\pi/5$, and assuming loss of half the coherence ($\lambda=0.5$). For H_2 in Fig. 9, the fit parameters are $\beta=\pi/6$ and $\lambda=0.5$ For both perturbers, fair agreement with the experiment is observed. This concerns in particular the marked propensity towards the $m_j'=+2$ sublevel of $6s6p\ ^3P_2$ in scattering of $6s6p\ ^1P_{1,m_j=+1}$ as well as the smaller cross section when barium is prepared in the $6s6p\ ^1P_{1,m_j=0}$ sublevel.

V. DISCUSSION

Alignment effects in singlet-triplet transfers collisionally induced by molecules have been examined by Bussert and Leone in the case $\mathrm{Ca}(4s5p\ ^1P_1\rightarrow 4s5p\ ^3P_J)$ [24]. The final J level of $4s5p\ ^3P$ has not been resolved in that work. The cross section is 20% larger for π alignment of the $^1P_1$ orbital as compared to σ alignment for collision with H_2 and D_2. The alignment effect is of 15% with CO_2, and the preferential alignment is for preparation of the σ orbital. No alignment effect has been observed with N_2, O_2 and many other molecules [24].

The results of Figs. 7–9 can be used to provide the information about alignment effects. One just needs to sum up the five Zeeman cross sections corresponding to a given preparation of $6s6p\ ^1P_{1,m_j}$. An alignment effect is observed for N_2 and H_2, and in both cases the preference is for the π preparation of the $6s6p\ ^1P_1$ orbital. The magnitude of the effect is 67±38% for N_2 and for H_2 it is about 40%. These effects are very large when compared to what was found for the $\mathrm{Ca}(4s5p\ ^1P_1\rightarrow 4s5p\ ^3P_J)$ energy transfers [24]. There could be three reasons for this. First, transfer to a single $J=2$ of a ^3P_J manifold is considered in the present work, whereas transfer to non-J-selected ^3P_J is considered in the previous work by Bussert and Leone [24]. Second, the $6s6p\ ^1P_1$ level of barium is very well separated from neighboring levels ($6s6p\ ^3P_2$ is the closest, and it is at 4546 cm^{-1}), whereas the $4s5p\ ^1P_1$ of calcium is only 156 cm^{-1} above the $4s5p\ ^3P_2$. The third reason is that no reactive channel is opened for collision of $\mathrm{Ba}(6s6p\ ^1P_1)$ with N_2 and H_2, whereas reaction forming CaN and CaH is possible in the case of $\mathrm{Ca}(4s5p\ ^1P_1)$ because of the large excitation of calcium. Leone indeed makes a link between the lack of an alignment effect and the possibility of a reactive channel [3,24].

The previous section has opened up the pathway for discussion of the physical phenomena that induce differences between Zeeman cross sections in Ba-N_2,H_2 scattering. The discussion following is organized so that it clarifies the kind of information provided by the present m_j selected cross sections compared to that brought by the more widely reported experiments on *polarization effects* where alignment is controlled in the entrance channel only. This discussion will concentrate on Ba-N_2 scattering, but most of it applies for Ba-H_2 as well. We shall then discuss the Ba-O_2 scattering in a qualitative way. This will allow a final look at those physical phenomena that play an important role for observing large polarization effects.

Standard experiments on the polarization effect have focused most of the attention on alignment effects in the entrance channel on total cross sections. The work of Leone and co-workers reported above, for $\mathrm{Ca}(4s5p\ ^1P_1)$ scattering, enters into this class of experiments. This corresponds to selection of $|m_j|$ in the entrance channel. Existence of an alignment effect in energy transfer cross sections is the result of two physical phenomena: (i) the couplings that are responsible for the $^1P_1\rightarrow{}^3P_2$ inelastic transfer are stronger on one of the two entrance curves, either that correlating to $m_j=\pm1$ (π-type preparation of the $^1P_1$ orbital) or that correlating to $m_j=0$ (σ-type preparation), and (ii) incomplete depolarization of the asymptotically selected orbital when the molecular axis rotates before locking. We have seen above that a significant alignment effect is observed in the Ba-N_2 collision that favors π-type preparation. This indicates both that the strongest couplings responsible for the $\mathrm{Ba}(6s6p\ ^1P_1\rightarrow 6s6p\ ^3P_2)$ transfer are located on the potential curves correlating to $m_j=\pm1$, and that the scrambling due to molecular rotation is limited. It is actually what was suggested by the model of Sec. IV.

Other types of experiments on polarization effects have brought attention to the orientation of the initial excited atomic orbital. This leads to left-right asymmetry in differential cross sections [32]. Of course, no information about this can be provided by the present work, which deals with total cross sections. However, the shape of the Doppler profiles in the probe laser induced fluorescence signals reflects the angular distribution of the product when the probe laser operates under the nonsaturation regime [25]. Under a geometry where the magnetic field was perpendicular to both the relative velocity and the probe laser direction, left-right asymmetry in the scattering would appear as nonsymmetrical Doppler profiles. A very small effect is expected, especially with molecular perturbers, and no attempt was made to obtain this geometry and investigate the corresponding effect.

Let us discuss now the polarization of the final level, $6s6p\ ^3P_2$. Examination of Fig. 7 shows that the $\mathrm{Ba}(6s6p\ ^1P_1)$–N_2 collision does not result in alignment of the final level $6s6p\ ^3P_2$. The alignment induced collisionally into $6s6p\ ^3P_2$ is indeed $\rho(^3P_2)_0=+0.02$ for initial preparation of $6s6p\ ^1P_{1,m_j=0}$ and -0.02 for preparation of $6s6p\ {}^1P_{1,m_j=+1}$, whereas this quantity takes the values $+0.53$ or -0.53 when the $6s6p\ {}^3P_2$ level is fully aligned into $m_j=\pm1$ or 0, respectively [33]. This lack of alignment of the product indicates that initial alignment of the reactants is lost during the collision. This is the result of scrambling between m_j sublevels due to the rotation of the molecular axis when the atomic orbital is not locked to it. The calculations reported in Fig. 7 predict a larger absolute value of the alignment than observed experimentally (about -0.06 for preparation of both $m_j=0$ and $+1$ of $6s6p\ {}^1P_1$ for both straight and bent trajectories), showing that not enough scrambling is predicted by the model.

For symmetry reasons, collision of the nonoriented $6s6p\ {}^1P_{1,m_j=0}$ orbital cannot result in an oriented final state $6s6p\ {}^3P_2$. It is actually what is observed in Fig. 7. In contrast, collisions of the oriented $6s6p\ {}^1P_{1,m_j=+1}$ orbital can and actually very slightly does result in oriented $6s6p\ {}^3P_2$. A value of 0.06 is found experimentally for the orientation coefficient $\rho({}^1P_1)_0$ [33]. This is about 10% of the largest possible value for this coefficient. The calculations reported in Fig. 7 predict a value of about 0.08, which is in fair agreement with the experiment. The reason why part of the initial orientation is transferred by the collision into the final state has been examined in Sec. IV. It is the result of incomplete loss of coherence when the collision proceeds along two potential curves that would be degenerate under $C_{\infty v}$ symmetry, but the degeneracy is lifted by the anisotropy of the Ba-N_2 interaction. The fit to experimental data shown in Fig. 7 assumes half conservation of the coherences (the parameter λ is set to 0.5 in the calculation).

The above analysis applies fully to the Ba-H_2 scattering. The predictions of the model are in fair agreement with the experimental results of Fig. 9, as it was the case for N_2. In contrast to N_2, full conservation of the coherences leads to a better fit of the experimental results than half conservation of it. The reason might be the smaller anisotropy of the molecule H_2 compared to N_2.

Examination of Fig. 10 makes the Ba+H_2 collision very interesting. It shows that the shape of the flux-velocity contour map of Ba($6s6p\ {}^3P_2$) depends on the magnetic sublevel in the product Ba($6s6p\ {}^3P_2$). The relation between the shape of the Doppler profile and the differential cross section is discussed in Ref. [25]. The bell shape profile for the formation of $6s6p\ {}^3P_{2,m_j'=0,-1}$ indicates forward or backward scattering, whereas the shape of the Doppler profile for the formation of $6s6p\ {}^3P_{2,m_j'=+2}$ suggests that the differential cross section is sideways peaked. The simple model of Sec. IV is not suited at all to account for such effects, but the importance of the effect should be a strong motivation for future development of a detailed theoretical treatment of the Ba-H_2 collision. If using the language of vector correlations, such an m_j,m_j'-dependent differential cross section corresponds to a 4-vector correlation study.

Let us end the discussion with Ba-O_2 scattering. When switching from N_2 to O_2, we switch from an inelastic process where close collisions dominate to an inelastic process where large impact parameter collisions and near-resonant energy transfer are important. This picture has been revealed when measuring the flux-velocity contour map of Ba($6s6p\ {}^3P_2$) in the $6s6p\ {}^1P_1 \rightarrow 6s6p\ {}^3P_2$ inelastic collision [25]. Such a difference in the collision dynamics certainly makes the scrambling of orbital polarization very different with O_2 as compared to N_2. For this reason, polarization effects are expected to be different with O_2 and N_2. However, this is not the reason why there is no observation of a polarization effect with O_2. On the contrary, scrambling of orbital polarization due to molecular rotation is probably less important with O_2 than with N_2. Another and more important difference exists between O_2 and N_2 that changes completely the nature of the coupling responsible for the $6s6p\ {}^1P_1 \rightarrow 6s6p\ {}^3P_2$ energy transfer. The ground state of O_2 is ${}^3\Sigma_g^-$, whereas that of N_2 is ${}^1\Sigma_g^+$. As a result, curves of both symmetries A' and A'' correlate to each magnetic sublevel of levels $6s6p\ {}^1P_1$ and $6s6p\ {}^3P_2$ in C_s geometry. Moreover, O_2 has a positive electron affinity that allows formation of the $Ba^+O_2^-$ intermediate that is also associated with curves of both A' and A'' symmetries [34]. The number of couplings between singlet and triplet curves through the ion-pair intermediate is thus very large and mixes the surfaces correlating to all the magnetic sublevels of $6s6p\ {}^1P_1$ and $6s6p\ {}^3P_2$. It is thus not surprising to observe in Fig. 8 that the cross sections $\sigma(6s6p\ {}^1P_{1,m_j} \rightarrow 6s6p\ {}^3P_{2,m_j'})$ are all equal, showing that no alignment and no orientation is transferred to $6s6p\ {}^3P_2$, no matter what the initial preparation of $6s6p\ {}^1P_1$.

VI. CONCLUSION

This investigation reports on a crossed-beam measurement of Zeeman cross sections $\sigma({}^1P_{1,m_j} \rightarrow {}^3P_{2,m_j'})$ for the spin-changing transition $6s6p\ {}^1P_1 \rightarrow 6s6p\ {}^3P_2$ induced by collisions with the molecular perturbers N_2, O_2, H_2. State-selective preparation of $6s6p\ {}^1P_{1,m_j}$ and detection of $6s6p\ {}^3P_{2,m_j'}$ was achieved using a magnetic field, which broke the degeneracy of the magnetic sublevels.

The results show that the Zeeman cross sections $\sigma({}^1P_{1,m_j} \rightarrow {}^3P_{2,m_j'})$ are fairly dependent upon m_j and m_j' for N_2 and H_2, whereas the Zeeman cross sections all have the same value with O_2. Additionally, the flux-velocity contour map of Ba($6s6p\ {}^3P_{2,m_j'}$) for scattering with H_2 depends significantly upon the value of m_j'. This is a very interesting result in its own.

A model is proposed that allows an interpretation of the observed cross sections. This model is based on a simple estimate of the Ba-(N_2,H_2) interaction potential. It takes into account of the depolarization effects in both the entrance and exit channels that are due to the rotation of the molecular axis. The spin-changing transition (${}^1P_1 \rightarrow {}^3P_2$) appears to be due to crossings between singlet curves that correlate to ${}^1P_{1,m_j=\pm1}$ and triplet curves that correlate to ${}^3P_{2,m_j=0,\pm1}$. This model has lead to a semiquantitative understanding of the difference observed between Zeeman cross sections in the Ba-N_2,H_2 scattering.

Finally, the discussion of scattering by O_2 has shown that absence of measurable polarization effects is not necessarily due to losses of orbital polarization in some complicated molecular rotations. It may be due simply to numerous couplings that act between potential surfaces correlating to all magnetic sublevels of both the entrance and exit levels.

ACKNOWLEDGMENTS

This work was partly supported by the NATO under Grant No. 99/89. Dr. A. J. Bell is acknowledged for his careful reading of the manuscript.

APPENDIX A: COHERENT SATURATION AND OPTICAL PUMPING IN THE PROBE

The detection of the barium atoms scattered in the $6s6p\ {}^3P_2$ level is a laser-induced-fluorescence (LIF) measurement. It is performed under a coherent saturation regime. Such a regime is actually very easily reached with the power of the cw dye lasers that are currently available (power densities of 10 mW/cm^2 can be reached with our experiment arrangement).

Billy *et al.* have recently examined the effect of coherent saturation on LIF measurements [35]. In particular, they have shown that the LIF signal is proportional to the Rabi pulsation in this case. The Rabi frequency ω_1 is given by

$$\omega_1 = -\langle 6s7s\ {}^3S_1, m_j'' | \vec{D}\cdot\vec{\epsilon}_q | 6s6p\ {}^3P_2, m_j' \rangle E_q/\hbar \tag{A1}$$

where $\vec{\epsilon}_q$ is the polarization vector of the laser electric field, E_q is its magnitude, and $\vec{D}$ is the dipole moment of the atom. Expression (A1) is written for the probe laser tuned to the transition $6s6p\ {}^3P_2, m_j' \rightarrow 6s7s\ {}^3S_1, m_j''$. The dipole moment of this transition is $\langle 6s7s\ {}^3S_1, m_j'' | \vec{D}\cdot\vec{\epsilon}_q | 6s6p\ {}^3P_2, m_j' \rangle$. It is given by [28]

$$\langle 6s7s\ {}^3S_1, m_j'' | \vec{D}\cdot\vec{\epsilon}_q | 6s6p\ {}^3P_2, m_j' \rangle = (-1)^{1-m_j''} \langle 6s7s\ {}^3S_1 \| D \| 6s6p\ {}^3P_2 \rangle \times \begin{bmatrix} 1 & 1 & 2 \\ -m_j'' & q & m_j' \end{bmatrix} . \tag{A2}$$

The quantity $\langle 6s7s\ {}^3S_1 \| D \| 6s6p\ {}^3P_2 \rangle$ is the reduced dipole moment of the transition $6s6p\ {}^3P_2 \rightarrow 6s7s\ {}^3S_1$. It does not depend on the initial and final magnetic quantum numbers m_j' and m_j''. The dependence on m_j' and m_j'' is only contained in the $3j$ coefficient

$$\begin{bmatrix} 1 & 1 & 2 \\ -m_j'' & q & m_j' \end{bmatrix}$$

in which q takes the values 0, +1 and −1 according to the polarization of the laser photons, whether it is linear, clockwise, or counterclockwise circular, respectively.

From expressions (A1) and (A2) it appears that the LIF signal is proportional to E_q, i.e., it is proportional to the square root of the power density P_q of the laser at the photon polarization q (P_0 is one-half of the total power density of the laser, and P_{+1} and P_{-1} are both one-quarter of it). It is also proportional to the $3j$ coefficient [36]

$$\begin{bmatrix} 1 & 1 & 2 \\ -m_j'' & q & 2m_j' \end{bmatrix} .$$

We have checked that the present experiment operates under the coherence saturation regime by varying the power density of the laser between 0.75 and 14 mW/cm^2. The result is shown in Fig. 13. The probe laser was tuned to the transition $6s6p\ {}^3P_2, m_j' = -2 \rightarrow 6s7s\ {}^3S_1, m_j'' = -1$. The LIF signal is actually proportional to the square root of the laser power above 1 mW/cm^2 power density.

After accounting for the efficiency of the probe laser excitation, we must examine the efficiency of the photon detection. Consider that the probe laser is tuned to the transition $6s6p\ {}^3P_2, m_j' \rightarrow 6s7s\ {}^3P_1, m_j''$ as shown in Fig. 14 (the figure shows the case $m_j' = +2$ with the detection tuned to the $6s7s\ {}^3S_1 \rightarrow 6s6p\ {}^3P_0$ transition). The excited atoms decay almost exclusively to the $6s6p\ {}^3P$ multiplet. Three possibilities must be considered for the decay:

(i) Decay through the transition on which the monochromator is tuned. The emitted photon is detected and the atom will never interact again with the probe laser. The emission coefficient for this is A_a as labeled in Fig. 14.

(ii) Decay to the same Zeeman sublevel of $6s6p\ {}^3P_2$ as the one probed. No photon is detected, but the atom can interact again with the laser and can be detected. The corresponding emission coefficient is A_b.

(iii) Decay to any other level than in (i) and (ii). No photon is detected. The atom does not interact any more

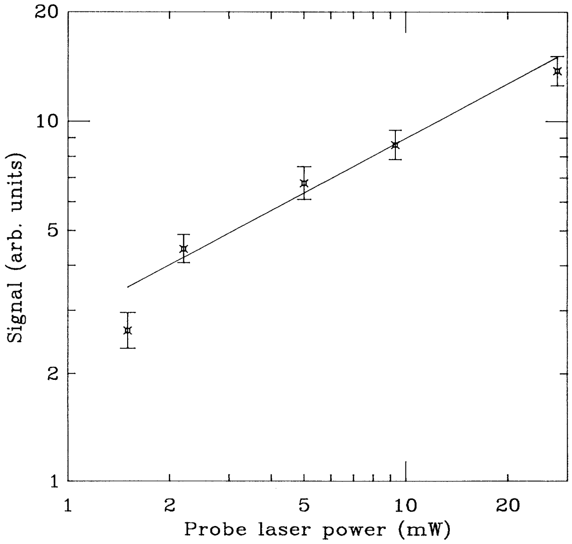

FIG. 13. Dependence of the detected signal on the power of the probe laser. The scale is log-log, and the straight line corresponds to a linear dependence of the signal upon the square root of the laser power.

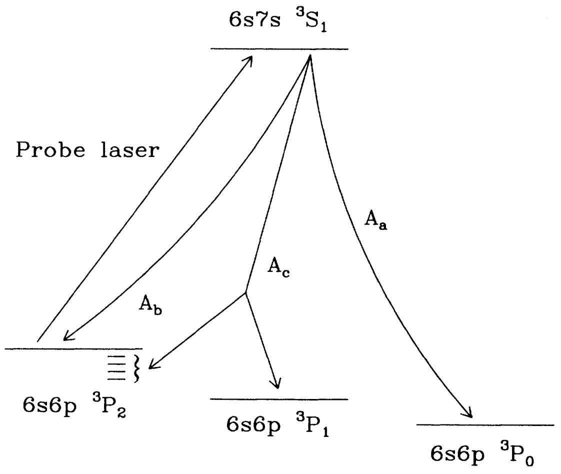

FIG. 14. Energy levels of barium showing the optical pumping phenomenon discussed in Appendix A.

with the probe laser. The emission coefficient is then A_c. The efficiency of the detection is then given by

$$f=\frac{A_a}{A_a+A_c} . \tag{A3}$$

Emission coefficients are easily deduced from the general expression of Einstein emission coefficients for the transitions $^3S_{1m_j''}\rightarrow{}^3P_{Jm_j'}$. Under pure LS coupling, they are given by [28]

$$A(^3S_{1m_j''}\rightarrow{}^3P_{Jm_j'})=A(^3S\rightarrow{}^3P)(2J+1)\langle Jm_j'1q|1m_j''\rangle^2 \times\begin{Bmatrix}1 & J & 1\\ 1 & 0 & 1\end{Bmatrix}^2 . \tag{A4}$$

Taking expressions (A1)–(A4) into account, we obtain the efficiencies for the LIF detection that are listed in Table I. These quantities are noted $\phi(m_j',J)$. They depend both on the magnetic sublevel m_j' of $6s6p\ ^3P_2$ that was probed, and on the final level $6s6p\ ^3P_J$ to which the $6s7s\ ^3S_1\rightarrow 6s6p\ ^3P_J$ detection was tuned.

The values of detection efficiencies $\phi(m_j',J)$ listed in Table I and used in Eq. (1) were checked experimentally by populating the Zeeman sublevels of $6s6p\ ^3P_2$ in a known fashion by radiative cascade. A single-mode dipole laser was tuned to the $6s6p\ ^1P_1\rightarrow 6s6d\ ^3D_2$ transition at 788.0 nm, and allowed us to pump selectively one magnetic sublevel of the $6s6d\ ^3D_2$ level (see Fig. 2). The radiative decay $6s6d\ ^3D_2\rightarrow 6s6p\ ^3P_2$ populates the Zeeman sublevel of $6s6p\ ^3P_2$ according to the square of Clebsch-Gordon coefficients. Detection of these populations using the probe laser allowed us to measure the detection efficiency of each Zeeman sublevel of $6s6p\ ^3P_2$. The results are shown in Table I and are compared to the efficiencies calculated using expressions (A1)–(A4) above. A nice agreement is observed between measurements and calculation. The experimental results have a limited accuracy of ±15% only because of the large instability of the diode laser at the tuning wavelength. Consequently, the calculated efficiencies have been preferred to extract the population of $6s6p\ ^3P_2$ Zeeman sublevels from the measured signals.

APPENDIX B: POTENTIAL CURVES OF THE Ba($6s6p\ ^{1,3}P$)–N_2 SYSTEM

This appendix shows how the approach described by Hickman for alkali metal ($np\,^2P$)-H_2,N_2 systems [29] was applied to the Ba($6s6p\ ^1P$)–N_2 and Ba($6s6p\ ^3P$)–N_2 pairs. All the notation closely follows that of Hickman.

The potential curves for Ba($6s6p\ ^1P$)-N_2 were obtained by diagonalizing the following Hamiltonian:

$$\begin{bmatrix} E_\Pi & 0 & \dfrac{H_{xx}-H_{yy}}{2}\\ 0 & E_\Sigma & 0\\ \dfrac{H_{xx}-H_{yy}}{2} & 0 & E_\Pi \end{bmatrix} , \tag{B1}$$

here defined by the basis

$$|1\rangle=|6s6p\ ^1P_{1,m_j=-1}\rangle ,$$
$$|2\rangle=|6s6p\ ^1P_{1,m_j=0}\rangle , \tag{B2}$$
$$|3\rangle=|6s6p\ ^1P_{1,m_j=+1}\rangle .$$

The construction of this Hamiltonian is a straightforward extension of the work of Hickman, and uses simple angular algebra. The quantities E_Σ and E_Π in expression (B1) are the potential curves describing Ba($6s6p\ ^1P_1$) in interaction with a rare-gas perturber. The Cs($6p$)-Ar potentials calculated by Pascale and Vandeplanque were used as an estimate of these quantities [37] (cesium is about the same size as barium).

The term $(H_{xx}-H_{yy})$ in (B1) deserves some comment. It is written to be consistent with the notation provided by Hickman in Fig. 1 of Ref. [29]. It refer to a Cartesian reference frame where the Ba-N-N atoms in C_s symmetry define the yz plane. The z direction is pointing from Ba to the center of mass of N_2, and the x direction is perpendicular to the Ba-N_2 molecular plane. In the work of Hickman, the term $(H_{xx}-H_{yy})$ accounts for the anisotropic interaction of the alkali-metal $np\ ^2P$ orbital with N_2. On average, when N_2 is rotated in the yz plane, the np_x and np_y orbitals do not interact in the same way with N_2. In the present work, alkali-metal ($np\ ^2P$) atoms were replaced with Ba($6s6p\ ^{1,3}P$). The term $(H_{xx}-H_{yy})$ then describes the anisotropy of the interaction between Ba and N_2. It was modeled by considering the possibility that the excited orbital $6p$ of Ba overlaps the lowest antibonding orbital of N_2. The overlap integral is nonzero and leads to a strong attraction when $6p$ and N_2 are parallel or approximately parallel (A' symmetry under the point group C_s). Otherwise it is zero, and no attraction occurs. When N_2 is rotated in the yz plane, the average overlap integral of the $6p$ and N_2 is zero for $6p_x$, and it is nonzero for $6p_y$. The term $(H_{xx}-H_{yy})$ was thus given the form

$$H_{xx} - H_{yy} = C \exp(-R/R_0) \ . \tag{B3}$$

In Eq. (B3), R is the approach distance of Ba and N_2. The strength C and the width R_0 of this interaction were chosen so that the attractive well in the lowest $^1A'$ curve has a reasonable well of 1500 cm^{-1}, i.e., about the same depth as that calculated by Habitz for the $Na(3p3\ ^2P)-N_2$ pair [38].

The picture provided above to justify the form given to the term $(H_{xx} - H_{yy})$ is directly consistent with the *ab initio* calculation of Habitz on the $Na(3p3\ ^2P)-N_2$ system [38]. Comparing the interaction of $Ba(6s6p\ ^{1,3}P)$ with N_2 to that of $Na(3p3\ ^2P)$ is relevant here, first because both have a similar ionization potential of about 3 eV, and secondly because the attractive part of the $Ba(6s6p\ ^{1,3}P)-N_2$ interaction is dominated by the interaction of the p electron.

The potential curves correlating to $Ba(6s6p\ ^3P_j)$ were obtained from a similar matrix diagonalization. In this case, however, the Hamiltonian was a 9×9 matrix projected onto the vectors $|6s6p\ ^3P_{j,m_j}\rangle$. Again, here it was derived after simple calculation of angular algebra from the work of Hickman. The input functions E_Σ and E_Π, as well as the input parameters C and R_0, were the same as for $Ba(6s6p\ ^1P_1)$ above.

The matrix diagonalizations that were performed numerically provided us with 3+9 energy levels and eigenvectors for each separation of the Ba-N_2 pair. This allowed us to draw the potential curves correlating to $Ba(6s6p\ ^1P_1)$ and $Ba(6s6p\ ^3P_j)$ that are shown in Fig. 11(b).

---

*Present address: C.E.N. Saclay, DSM/DRECAM/SCM, 91191 Gif-sur-Yvette CEDEX, France.

†Present address: Baker Laboratory, Dept. of Chemistry, Cornell University, Ithaca, NY 14853.

[1] I. V. Hertel, H. Schmidt, A. Bähring, and E. Meyer, Rep. Prog. Phys. **48**, 375 (1985).

[2] E. E. B. Campbell, H. Schmidt, and I. V. Hertel, Adv. Chem. Phys. **72**, 37 (1988).

[3] S. R. Leone, in *Selectivity in Chemical Reactions*, edited by J. C. Whitehead, Vol. 245 of NATO ASI Ser. C (Kluwer, Dordrecht, 1988), pp. 245–263.

[4] P. S. Weiss, M. H. Covinsky, H. Schmidt, B. A. Balko, Y. T. Lee, and J. M. Mestdagh, Z. Phys. D. **10**, 227 (1988).

[5] H. A. J. Meijer, T. J. C. Pelgrim, H. G. M. Heideman, R. Morgenstern, and N. Andersen, J. Chem. Phys. **90**, 738 (1989).

[6] J. P. J. Driessen, F. J. M. v. d. Weijer, M. J. Zonneveld, L. M. T. Somers, M. F. M. Janssens, H. C. W. Beijerinck, and B. J. Verhaar, Phys. Rev. Lett. **62**, 2369 (1989); **64**, 2106 (1989); Phys. Rev. A **42**, 4058 (1990); M. P. I. Manders, W. B. M. van Hoek, E. J. D. Vredenbregt, G. J. Sandker, H. C. W. Beijerinck, and B. J. Verhaar, *ibid.* **39**, 4467 (1989).

[7] H. Hülser, E. E. B. Campbell, R. Witte, H. Genger, and I. V. Hertel, Phys. Rev. Lett. **64**, 392 (1990).

[8] R. L. Robinson, L. J. Kovalenko, and S. R. Leone, Phys. Rev. Lett. **64**, 388 (1990).

[9] R. L. Robinson, L. J. Kovalenko, C. J. Smith, and S. R. Leone, J. Chem. Phys. **92**, 5260 (1990).

[10] M. P. I. Manders, W. M. Ruyten, F. v. d. Beucken, J. P. J. Driessen, W. J. T. Veugeler, P. H. Kramer, E. J. D. Vredenbregt, W. B. M. van Hoek, G. J. Sandker, H. C. W. Beijerinck, and B. J. Verhaar, J. Chem. Phys. **89**, 4777 (1988).

[11] A. G. Suits, H. T. Hou, H. F. Davis, Y. T. Lee, and J. M. Mestdagh, J. Chem. Phys. **95**, 8178 (1991).

[12] J.-C. Gay and W. B. Schneider, Z. Phys. A **278**, 211 (1976); Phys. Rev. A **20**, 879 (1979); **20**, 894 (1979); **20**, 905 (1979).

[13] R. Boggy and F. A. Franz, Phys. Rev. A **25**, 1887 (1982).

[14] P. Skalinski and L. Krause, Phys. Rev. A **26**, 3338 (1982).

[15] R. W. Berends, P. Skalinski, and L. Krause, J. Phys. B **17**, 605 (1984).

[16] R. W. Berends, W. Kedzierski, and L. Krause, Phys. Rev. A **37**, 68 (1988).

[17] M. Baba and H. Katô, J. Chem. Soc. Faraday Trans. **85**, 965 (1989).

[18] J. P. J. Driessen, H. J. L. Megens, M. J. Zonneveld, H. A. J. Senhorst, H. C. W. Beijerinck, and B. J. Verhaar, Chem. Phys. **147**, 447 (1990).

[19] W. H. Breckenridge and C. N. Merrow, J. Chem. Phys. **88**, 2329 (1988).

[20] J. P. Visticot, J. Berlande, J. Cuvellier, J. M. Mestdagh, P. Meynadier, P. de Pujo, O. Sublemontier, A. J. Bell, and J. G. Frey, J. Chem. Phys. **93**, 5354 (1990).

[21] J. P. Visticot, P. de Pujo, O. Sublemontier, A. J. Bell, J. Berlande, J. Cuvellier, T. Gustavsson, A. Lallement, J. M. Mestdagh, P. Meynadier, and A. G. Suits, Phys. Rev. A **45**, 6371 (1992).

[22] M. H. Alexander and B. Pouilly, J. Chem. Phys. **90**, 5373 (1989).

[23] B. Pouilly and M. H. Alexander, Chem. Phys. **145**, 191 (1990).

[24] W. Bussert and S. R. Leone, Chem. Phys. Lett. **138**, 269 (1987).

[25] A. Suits, P. de Pujo, O. Sublemontier, J.-P. Visticot, J. Berlande, J. Cuvellier, T. Gustavsson, J.-M. Mestdagh, P. Meynadier, and Y. T. Lee, Phys. Rev. Lett. **67**, 3070 (1991); J. Chem. Phys. **97**, 4094 (1992).

[26] C. J. Smith, J. P. J. Driessen, L. Eno, and S. R. Leone, J. Chem. Phys. **96**, 8212 (1992).

[27] J. Cuvellier, J. M. Mestdagh, J. Berlande, P. de Pujo, and A. Binet, Rev. Appl. Phys. **16**, 679 (1981); J. M. Mestdagh, J. Berlande, J. Cuvellier, P. de Pujo, and A. Binet, J. Phys. B **15**, 439 (1982).

[28] R. D. Cowan, *The Theory of Atomic Spectra* (University of California, Berkeley, 1981).

[29] A. P. Hickman, J. Phys. B **15**, 3005 (1982).

[30] G. C. Schatz, L. J. Kovalenko, and S. R. Leone, J. Chem. Phys. **91**, 6961 (1989).

[31] D. M. Brink and G. R. Satchler, *Angular Momentum* (Clarendon, Oxford, 1975).

[32] R. Düren and E. Hasselbrink, J. Chem. Phys. **85**, 1880 (1986).

[33] The longitudinal orientation ($k=1$) and alignment ($k=2$) coefficients are calculated using the general formula $\rho_0^k = \sum_M (-1)^{J-M} \langle J,J,M,-M|k,0\rangle \rho_{M,M}$, where J is the

orbital momentum of the level under consideration, and M its projection along the quantization axis, and where $\rho_{M,M}$ is the population of the $|JM\rangle$ state. A very good account of density matrix algebra is given by A. Omont, Prog. Quantum Electron **5**, 69 (1977).

[34] A. A. Christodoulides, D. L. McCorkle, and L. G. Christophorou, in *Electron-Molecule Interactions and their Applications,* edited by L. G. Christophorou (Academic, New York, 1984), Vol. 2, p. 423.

[35] N. Billy, B. Girard, G. Gouédard, and J. Vigué, Mol. Phys. **61**, 65 (1987).

[36] If not operating under the regime of coherent saturation, the LIF signal would have been proportional to

$$P_q \begin{pmatrix} 1 & 1 & 2 \\ -m_j'' & q & m_j' \end{pmatrix}^2 .$$

[37] J. Pascale and J. Vandeplanque, J. Chem. Phys. **60**, 2278 (1974).

[38] P. Habitz, Chem. Phys. **54**, 131 (1980).